



Soft Matter

Lubricated Steady Sliding of a Rigid Sphere on a Soft Elastic Substrate: Hydrodynamic Friction in the Hertz limit

Journal:	<i>Soft Matter</i>
Manuscript ID	SM-ART-12-2019-002447.R1
Article Type:	Paper
Date Submitted by the Author:	13-Feb-2020
Complete List of Authors:	Wu, Haibin; Cornell University, Department of Mechanical and Aerospace Engineering Moyle, Nichole; Lehigh University, Jagota, Anand; Lehigh University, Bioengineering Hui, Chung-Yuen; Cornell University, Theoretical and Applied Mechanics

SCHOLARONE™
Manuscripts

Lubricated steady sliding of a rigid sphere on a soft elastic substrate: hydrodynamic friction in the Hertz limit

Haibin Wu,^a Nichole Moyle,^b Anand Jagota^b and Chung-Yuen Hui^{*a}

^a Department of Mechanical and Aerospace Engineering, Field of Theoretical and Applied Mechanics, Cornell University, Ithaca, NY 14853, USA

^b Departments of Bioengineering and of Chemical & Biomolecular Engineering, 111 Research Drive, Lehigh University, Bethlehem, PA 18015, USA

* corresponding author: C.-Y. Hui, E-mail: ch45@cornell.edu

Abstract:

Lubricated sliding on soft elastic substrates occurs in a variety of natural and technological settings. It very often occurs in the *iso-viscous* elasto-hydrodynamic lubrication (EHL) regime (e.g., soft solid, low pressure). In this regime, for sliding of a smooth sphere on a soft solid, a “Hertz-like” effective contact region forms. Much of the fluid is squeezed out of the contact region although enough is retained to keep the solid surfaces fully separated. This is accompanied by complex deformation of the soft solid. The behavior of such soft lubricated contacts is controlled by a single dimensionless parameter $1/\beta$ that can be interpreted as a normalized sliding velocity. Solving this fundamental soft-lubrication problem poses significant computational difficulty for large β , which is the limit relevant for soft solids. As a consequence, little is known about the structure of the flow field under soft lubrication in the intake and outlet regions. Here we present a new solution of this soft lubrication problem focusing on the “Hertz” limit. We develop a formulation in polar coordinates that handles difficult computational issues much better than previous methods. We study how hydrodynamic pressure, film thickness and hydrodynamic friction vary with β . Scaling laws for these relationships are given in closed form for a range of β not previously accessible theoretically but that is typical in applications. The computational method presented here can be used to study other soft lubrication problems.

1. Introduction

Lubricated sliding in which an intervening liquid layer separates two solid surfaces is ubiquitous in nature and in technology. When at least one of the solids is soft, we obtain an important subclass: Soft Lubrication or Elasto-Hydrodynamic Lubrication (EHL) ¹⁻³. Technological phenomena governed by soft lubrication include sliding of rubbery tires or shoe soles on a hard surface. Some parts of our body rely on soft lubrication to function; examples are joints, eyeballs, eyelids, and contact lenses. Lubricated elastic contacts have been extensively studied, traditionally with a heavy emphasis on stiff metal contacts such as in bearings ^{4,5} and pistons ^{6,7}. For more compliant materials the effect of deformation qualitatively alters the contact geometry and pressure profile, as well as hysteretic friction forces ⁸⁻¹². Typically, the EHL regime occurs when there is a continuous fluid film separating the contacting surfaces. Material compliance and lubricant viscosity strongly affect friction behavior in this regime. As velocity is decreased and load is increased, the system enters the boundary lubrication regime, where there are breaks in the

liquid film. Here adhesive forces form areas of dry contact as well as hysteretic forces from material deformation begin to contribute to the friction response. In this regime sample roughness and inelasticity control the friction behavior. The problem of liquid drainage for compliant contacts under lubricated conditions has been studied for both thick and thin compliant layers^{13–16}. Our focus in this work is on the low Hersey number range of the EHL or soft lubrication regime, i.e., under conditions such that the solid surfaces remain separated by a thin liquid film. In many of these cases we can additionally assume that the liquid is Newtonian with a constant viscosity (iso-viscous).

Specifically, we consider a basic problem: the lubricated sliding of a rigid sphere on a soft, flat, and elastic substrate in the iso-viscous EHL regime. This work was motivated by our recent experimental study of this problem¹⁷. Briefly, we slide a spherical glass indenter on the lubricated surface of a thick slab of polydimethylsiloxane (PDMS). These tests are performed using different combinations of sliding velocity, normal load and sphere radius. Our result shows that, consistent with EHL theory, suitably normalized hydrodynamic friction plotted against the normalized sliding velocity collapses to a master curve, which means that hydrodynamic lubrication is controlled by a single dimensionless parameter which is the normalized sliding velocity (defined later).

Many studies have examined lubricated sliding of compliant materials with a sphere-on-flat contact geometry to investigate the effects of properties such as material modulus, lubricant viscosity, bulk viscoelasticity, and surface roughness^{18–25}. All these works are based on the lubrication theory developed by Reynolds²⁶. The EHL problem requires the simultaneous solution of the Reynolds and the elasticity equations. Since the Reynolds equation is highly nonlinear, there is no analytical solution for the sphere-on-flat contact problem. EHL problems are solved numerically by discretizing the calculation domain and using the finite element or finite difference method to iteratively solve the Reynolds and elasticity equations until the liquid film reaches a stable shape and the hydrodynamic pressure balances the applied load^{27–29}. However, this problem has many numerical difficulties, especially in the EHL or soft lubrication regime. In this regime, the discretized Reynolds equation become ill-conditioned resulting in failure of standard methods^{29–31}. Another well-known numerical difficulty is the calculation of the elastic deformation^{32–35}. Standard methods bear tremendous computational cost because of the mathematical coupling between surface points. However, this is precisely the regime of interest for lubrication of soft solids, and where our experiments are carried out. No accurate solutions have been obtained for conditions that approach truly soft lubrication. The purpose of our work is to rectify this deficiency.

1.1 Brief background

To place our work in context, we begin with a brief description of the state of the art in solution of soft lubrication problems. In 1951, Petrusevich³⁶ devised the first successful numerical scheme to solve the problem of a 2D cylinder undergoing lubricated sliding on an infinite elastic substrate. However, his method only works for light loads. When solving the Reynolds equation, numerical instability usually occurs as the applied load increases. Typically, during iterations, the hydrodynamic pressure starts to oscillate in the direction of fluid flow, usually just upstream of the center of the contact region^{37–39}. For small applied normal loads, the oscillations gradually fade away and the solution converges. However, oscillations continue to build up at higher loads and the numerical scheme fails^{37,39}. Furthermore, the iteration number for convergence is larger for higher loads than the smaller loads. Since the deformation at each grid point depends on the contribution from every other grid point, the number of arithmetic operations for one iteration is on the order of n^2 where n is the number of nodes. This means for higher

loads, much more calculation time will be spent on the evaluation of elastic deformation. Due to these difficulties, the results of several previous studies were limited to light loading conditions^{30,40}. In 1959, Dowson and Higginson²⁸ introduced the inversed method for the line load problem and obtained solutions for higher loads. In a series of papers, Hamrock and Dowson^{29–31,41} introduced a forward iteration method to solve the problem of a rigid *sphere* undergoing lubricated sliding on an infinite elastic substrate, which is normally referred to as the point contact problem. However, their method could only tackle light to medium normal loads and failed when the sphere was subjected to large normal loads. Evan et. al^{38,39} extended the inverse method²⁸ to solve the point-contact problem for higher loads. However, this method is not autonomous as it requires considerable manual intervention. Many existing works focused on fluids which exhibit pressure-sensitive viscosity. This feature introduces extra physical parameters in the problem that are usually irrelevant for soft lubrication; as a result, it is difficult to develop universal scaling laws indicating how physical quantities such as applied normal load, sliding velocity, film thickness, viscosity, elastic modulus, radius of sphere, are related to each other. In addition, the role of pressure-sensitive viscosity is negligible for typical soft solids⁴². There is a need for a robust computational method to solve EHL problems in the regime where β is a large number ($\gg 100$) and fluid viscosity is constant. Here we mention a recent work of Putignano⁴³ who suggested a generalized numerical method to deal with lubricated contact between linear viscoelastic surfaces. The viscoelastic deformation of the surfaces was linearized as a function of hydrodynamic pressure and velocity of the two surfaces. The surfaces' viscoelastic deformation was further coupled to Reynold equation for full solution of hydrodynamic pressure and film thickness. His iteration scheme is similar to this present work except that we consider only elastic deformation.

Here we mentioned some related contact mechanics problems in the EHL regime. For example, Daddi-Moussa-Ider et al⁴⁴ obtained explicit analytic expressions for the lift force acting on a rigid sphere undergoing lubricated sliding on a finite elastic membrane by applying the Lorentz reciprocal theorem. Rallabandi et al⁴⁵ studied the rotation of a rigid cylinder sliding near a thin elastic coating and showed analytically that the angular velocity of the cylinder scales with the cube of the sliding speed.

More relevant is the fact that very little is known quantitatively about the structure of the pressure and flow fields near the intake and outlet regions of a sphere undergoing lubricated sliding in the “Hertz” limit of soft solids, high loads or slow sliding velocities. Here we note the work of Snoeijer et al⁴⁶ which carefully studied lubricated sliding of a rigid cylinder under Hertz conditions. They also provided limited results for the sphere case, which is the focus of this paper. For the soft solid/small sliding velocity/high load or “Hertz” regime, we need to develop a numerical scheme to study the behavior in this limit. In all previous works, the Reynolds equation and elasticity equation were solved in Cartesian coordinates. However, as the applied load increases, the liquid film thins, and the hydrodynamic pressure converges to the elastic Hertz pressure⁴⁷ except near the inlet and outlet region, where a boundary layer exists to smooth out the infinite pressure gradient of the Hertz solution. The disadvantage of a numerical set up in Cartesian coordinates is that there is no simple way to refine the mesh locally to capture the pressure spike (when it exists) or the pressure gradient (which is large, whether or not the viscosity is pressure sensitive).

In this work, we have developed a method to study the EHL problem well within the EHL limit. It is based on formulating the problem in polar coordinates. The numerical result of hydrodynamic friction matches the experimental data very well. We show that with suitable normalization, the problem depends on a single dimensionless variable that combines properties and parameters such as normal load,

velocity, compliance, and viscosity. We present results for the pressure field, gap thickness, and friction as closed-form functions of the dimensionless velocity.

The plan for this paper is as follows: Section 2 summarizes the formulation of EHL problem in polar coordinates, after which the focus shifts to numerical implementation. Section 3 presents the numerical results and comparison with the experimental data. We conclude with a summary and discussion in Section 4.

2. Governing equations of the iso-viscous EHL problem in cylindrical coordinates

The schematic of our problem is shown in Fig. 1. A rigid sphere of radius R is sliding to the right on the surface of an incompressible elastic substrate at a constant velocity, v . The surface of the substrate is lubricated by a liquid film. We assume *steady state sliding*, so all field quantities are invariant in time with respect with a coordinate system fixed to the rigid sphere. In the following we use a cylindrical coordinate system (r, θ, z) for this moving frame. Note that $z=0$ is the *undeformed* surface of the elastic substrate. The substrate has shear modulus G and is incompressible with Poisson's ratio 0.5. A constant normal displacement of h_0 (with respect to $z=0$) is imposed on the sphere.

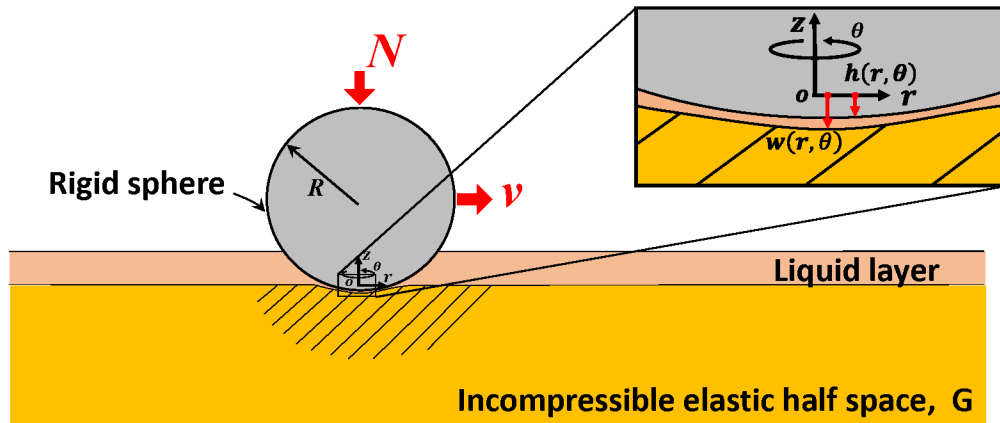


Fig. 1 A schematic of the EHL problem with an iso-viscous liquid layer

Let h denotes the z -coordinate of the surface of the moving sphere relative to the moving frame and let w denotes the vertical surface displacement of the elastic substrate from its undeformed configuration $z=0$. As usual, the surface of the rigid sphere is approximated by a paraboloid, i.e.,

$$h(r, \theta) = h_0 + \frac{r^2}{2R} \quad (1a)$$

where h_0 is the indentation depth which can be positive or negative. Positive h_0 corresponds to a small normal load. In this work we are mostly interested in $h_0 < 0$. The Reynolds equation for our problem is well known²⁹. For more details of the derivation of the Reynolds equation in our coordinates, see supporting information. In cylindrical coordinates, it is:

$$\frac{1}{r} \frac{\partial}{\partial r} \left(\frac{1}{12\eta} r \frac{\partial p}{\partial r} \cdot u^3 \right) + \frac{1}{r} \frac{\partial}{\partial \theta} \left(\frac{1}{12\eta} \frac{1}{r} \frac{\partial p}{\partial \theta} \cdot u^3 \right) = -\frac{v}{2} \left(\cos \theta \frac{\partial u}{\partial r} - \frac{\sin \theta}{r} \frac{\partial u}{\partial \theta} \right) \quad (1b)$$

where p is hydrodynamic pressure, η is the constant dynamic viscosity of the liquid and

$$u = h - w \quad (1c)$$

is the liquid film thickness. The substrate deformation caused by the hydrodynamic pressure is ⁴⁷:

$$w(r, \theta) = -\frac{1}{4\pi G} \int_0^{2\pi} \int_0^{\infty} \frac{p(r', \theta') r' dr' d\theta'}{\sqrt{(r \cos \theta - r' \cos \theta')^2 + (r \sin \theta - r' \sin \theta')^2}} \quad (2)$$

Here the linear elastic theory is used to calculate substrate's deformation. As shown by Lin et al.⁴⁸ the Hertz approximation based on linear theory is actually very good even for contact radius a up to 0.3 times sphere radius, R . In the experiments and in the simulations $a/R < 0.3$. Note that because normalized displacement of the surface, δ/R : $(a/R)^2$, so even fairly large contact radius corresponds to quite small surface displacements. Eqn (1a-c) and (2) completely specify the sliding problem and are to be solved with the boundary condition:

$$p(r \rightarrow \infty) = 0 \quad (3)$$

2.1 Normalization

We demonstrate that the solution is controlled by a single parameter by introducing the following normalization:

$$\bar{r} = \frac{r}{\sqrt{R|h_0|}}, \quad \bar{w} = \frac{w}{|h_0|}, \quad \bar{h} = \frac{h}{|h_0|}, \quad \bar{p} = \frac{p}{4\pi G \sqrt{|h_0|/R}}, \quad \bar{N} = \frac{N}{4\pi G |h_0| \sqrt{R|h_0|}} \quad (4)$$

This normalization is motivated by the classical result of Hertz contact theory where the contact radius a_H and the normal load N are related to the indentation depth $|h_0|$ by ⁴⁷:

$$a_H = \sqrt{R|h_0|} \quad \text{and} \quad N = \frac{16}{3} G |h_0| \sqrt{R|h_0|}, \quad (5a,b)$$

respectively. Recall that the Hertz pressure distribution p_H is axisymmetric and is given by

$$p_H(r) = \begin{cases} (8G/\pi) \sqrt{|h_0|/R} \sqrt{1-r^2/R|h_0|} & r \leq \sqrt{R|h_0|} \\ 0 & r > \sqrt{R|h_0|} \end{cases} \quad (5c,d)$$

In eqn (4), we have normalized the radial distance by the Hertz contact radius eqn (5a) and the normalized load by the Hertz load eqn (5b) to within a numerical constant.

The normalized forms of eqn (1) and (2) are:

$$\frac{1}{\bar{r}} \frac{\partial}{\partial \bar{r}} \left(\bar{r} \frac{\partial \bar{p}}{\partial \bar{r}} \cdot \bar{u}^3 \right) + \frac{1}{\bar{r}} \frac{\partial}{\partial \theta} \left(\frac{1}{\bar{r}} \frac{\partial \bar{p}}{\partial \theta} \cdot \bar{u}^3 \right) = -\frac{1}{\beta} \left(\cos \theta \frac{\partial \bar{u}}{\partial \bar{r}} - \frac{\sin \theta}{\bar{r}} \frac{\partial \bar{u}}{\partial \theta} \right) \quad (6a)$$

$$\bar{w} = - \int_0^{2\pi} \int_0^{\infty} \frac{\bar{p}(\bar{r}, \theta') \bar{r}' d\bar{r}' d\theta'}{\sqrt{(\bar{r} \cos \theta - \bar{r}' \cos \theta')^2 + (\bar{r} \sin \theta - \bar{r}' \sin \theta')^2}} \quad (6b)$$

where:

$$\bar{u} = \bar{h} - \bar{w}, \quad \bar{h} = -1 + \bar{r}^2 / 2, \quad (6c)$$

and β is the dimensionless parameter defined by

$$\beta = \frac{2 h_0^2 \pi G}{3 R \eta v}. \quad (6d)$$

Our normalization implies that the normalized normal load \bar{N} , normalized pressure \bar{p} and normalized film thickness \bar{u} have the form:

$$\bar{N} = \bar{N}(\beta), \quad \bar{p} = \bar{p}(\bar{r}, \theta, \beta), \quad \bar{u} = \bar{u}(\bar{r}, \theta, \beta) \quad (6e)$$

Eqn (6a) states that the solution is completely determined by a single dimensionless parameter β . If one interpret $1/\beta$ as a normalized sliding velocity, then the normalized normal load depends only on the normalized velocity and vice-versa. Our $1/\beta$ is equivalent to the dimensionless parameter λ_{3D} introduced by Snoeijer et al⁴⁶.

2.2 Hertz limit and asymptotic behavior of hydrodynamic pressure

Our experiments are in the regime of large β which corresponds to large normal indentation depths or slow velocities in (6d). In this regime, the pressure distribution is expected to converge to the Hertz pressure, eqn (5c), which in normalized form is:

$$\bar{p}_H = \begin{cases} \frac{2}{\pi^2} \sqrt{1 - \bar{r}^2}, & \bar{r} < 1 \\ 0, & \bar{r} \geq 1 \end{cases} \quad (7a,b)$$

However, the convergence cannot be uniform since the pressure gradient given by the Hertz theory is infinite and discontinuous according to eqn (7a,b) whereas the actual pressure should be continuously differentiable everywhere. Thus, there must exist an internal boundary layer, δ , at the inlet and outlet region. In normalized coordinates, this boundary layer is located at $\bar{r} = 1$. We anticipate the thickness of this boundary layer, $\bar{\delta} = \delta / \sqrt{R|h_0|}$, will vanish as $\beta \rightarrow \infty$. Also, we expect that, as $\beta \rightarrow \infty$, the film thickness \bar{u} goes to zero for all $\bar{r} < 1 - \bar{\delta}$. Thus,

$$\bar{u}(\bar{r} < 1 - \bar{\delta}, \theta, \beta \rightarrow \infty) \approx 0 \Rightarrow \bar{w}(\bar{r} < 1 - \bar{\delta}, \beta \rightarrow \infty) = -1 + \frac{\bar{r}^2}{2} \quad (8)$$

If we substitute eqn (8) into eqn (6b), then the pressure distribution given by eqn (7a) will satisfy eqn (2.8) for $\bar{r} < 1 - \bar{\delta}$. Note that since the Hertz pressure and its gradient are bounded for $\bar{r} < 1 - \bar{\delta}$, the PDE (2.6a) will be satisfied since $\bar{u}(\bar{r} < 1 - \bar{\delta}, \theta, \beta \rightarrow \infty) \rightarrow 0$. Hence, we expect that the Hertz pressure should prevail in $\bar{r} < 1 - \bar{\delta}$, and the fluid pressure should vanish rapidly for $\bar{r} > 1 + \bar{\delta}$.

The far field pressure for *any* $\beta > 0$ can be readily obtained using asymptotic methods. In the Appendix, we show that, to leading order, the pressure distribution for $\bar{r} \gg 1$ is given by

$$\bar{p}(\bar{r} \gg 1, \theta, \beta) = \frac{4}{5\beta\bar{r}^3} \cos\theta \quad (9)$$

Thus the pressure decays as the third power of distance from the indenter.

2.3 Discretization of the Reynolds Equation in polar coordinate

We choose our set-up in polar coordinates since it dramatically reduces the number of grid points needed. Physically, one expect that variation in the angular direction to be slow so the grid is dense only in the radial direction, especially near the exit and intake regions at $\bar{r} = 1$. Our numerical experiments have shown that a 50×30 (radial \times angular) mesh grid in polar coordinates could reach the same accuracy achieved by a 100×50 (x-direction \times y-direction) mesh grid in Cartesian coordinates while the calculation time in polar coordinates is about 10 *times* faster.

Since the solution has reflective symmetry about the vertical axis, only half of the domain $\theta \in [0, \pi]$ needs to be considered. A non-uniform mesh $\{\bar{r}_j\}$ is used in the radial direction whereas a uniform mesh $\theta_i = i\Delta\theta$ is employed in the θ direction. A schematic of the calculation domain is shown in the Fig. 2.

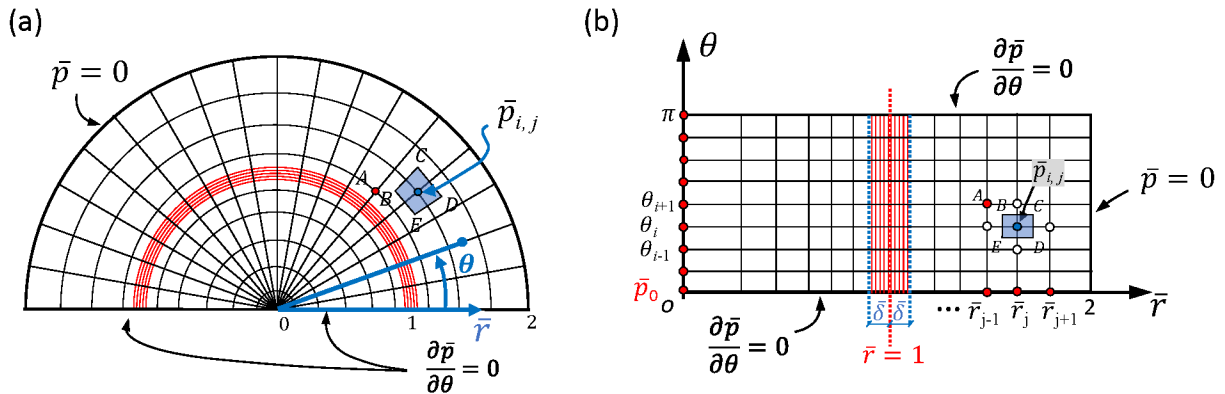


Fig. 2 (a) A schematic of the calculation domain and the mesh in cylindrical coordinate. Note mesh is much denser in the radial direction at $\bar{r} = 1$. (b) Mapping the semicircular calculation into a rectangular calculation domain, with the boundary condition being applied.

We use the finite difference method to solve eqn (6a). For the uniform mesh in the angular direction, we applied standard centered finite differences for the first and second derivatives, i.e.,

$$\left(\frac{\partial f}{\partial \theta}\right)_{i,j} = \frac{f_{i+1,j} - f_{i-1,j}}{2\Delta\theta}, \quad \left(\frac{\partial^2 f}{\partial \theta^2}\right)_{i,j} = \frac{f_{i+1,j} - 2f_{i,j} + f_{i-1,j}}{(\Delta\theta)^2} \quad (10a,b)$$

For the non-uniform mesh in the radial direction, the finite difference for the first and second order derivatives are obtained from the Taylor expansion:

$$\left(\frac{\partial f}{\partial r}\right)_{i,j} = \frac{f_{i,j+1} - \lambda_j^2 f_{i,j-1} - (1 - \lambda_j^2) f_{i,j}}{d_j (1 + \lambda_j)} \quad (11a)$$

$$\left(\frac{\partial^2 f}{\partial r^2}\right)_{i,j} = \frac{2[f_{i,j+1} + \lambda_j f_{i,j-1} - (1 + \lambda_j) f_{i,j}]}{d_j d_{j-1} (1 + \lambda_j)} \quad (11b)$$

$$\text{where: } d_j = \bar{r}_{j+1} - \bar{r}_j, \quad \lambda_j = d_j / d_{j-1} \quad (11c)$$

To ensure that the finite difference of the first and second derivatives in the radial direction preserves 2nd order accuracy, a special arrangement of non-uniform mesh is selected as suggested by ⁴⁹, i.e.,

$$\lambda_j = 1 + \frac{a}{L} \left(\frac{L - \bar{r}_j}{L}\right)^b d_{j-1}, \quad (12)$$

where L is the length of the radial segment where the non-uniform mesh is deployed, a and b are two coefficients to control the mesh interval size. In this work, we selected $b=0$ and adjust a to ensure that the grid number of the radial segment reaches the desired value.

Substituting eqn (10), (11) into (6a), we obtained the discretized version of eqn (6a)

$$A_{i,j} p_{i-1,j} + B_{i,j} p_{i,j-1} + C_{i,j} p_{i,j} + D_{i,j} p_{i,j+1} + E_{i,j} p_{i+1,j} = F_{i,j} \quad (13)$$

The coefficients $A_{i,j}, B_{i,j}, C_{i,j}, D_{i,j}, E_{i,j}$ and $F_{i,j}$ are functions of mesh spacing, normalized liquid film thickness and β . They are given in the Appendix.

The singular point $\bar{r} = 0$ requires special numerical attention. Specifically, the singularity at $\bar{r} = 0$ is regularized by integrating both sides of eqn (6a) over a small circular domain D centered at origin, i.e.,

$$\iint_D \nabla \cdot (\nabla \bar{p} \cdot \bar{u}^3) dA = \iint_D \frac{-1}{\beta} \left(\cos \theta \frac{\partial \bar{u}}{\partial \bar{r}} - \frac{\sin \theta}{\bar{r}} \frac{\partial \bar{u}}{\partial \theta} \right) dA \quad (14)$$

Applying divergence theorem to the left-hand side (LHS) of eqn (14), we obtained

$$\int_{\partial D} \bar{u}^3 \frac{\partial \bar{p}}{\partial r} ds = \iint_D \frac{-1}{\beta} \left(\cos \theta \frac{\partial \bar{u}}{\partial \bar{r}} - \frac{\sin \theta}{\bar{r}} \frac{\partial \bar{u}}{\partial \theta} \right) dA \quad (15)$$

We use finite difference scheme to evaluate both sides of eqn (15). This allows us to solve for the pressure \bar{p}_0 at $\bar{r} = 0$, which is eqn (16). The details of derivation from eqn (15) to (16) is shown in SI.

$$\bar{p}_0 = \frac{\sum_{i=0}^m (\bar{u}_0^3 + \bar{u}_{i,1}^3) \bar{p}_{i,1}}{\sum_{k=0}^m (\bar{u}_0^3 + \bar{u}_{k,1}^3)} + \frac{\Delta \bar{r}_1}{2\beta \sum_{k=0}^m (\bar{u}_0^3 + \bar{u}_{k,1}^3)} \left[\sum_{k=0}^m \cos \theta_k (\bar{u}_{k,1} - \bar{u}_0) - \sum_{k=1}^{m-1} \sin \theta_k \frac{(\bar{u}_{k+1,1} - \bar{u}_{k-1,1})}{\Delta \theta} \right] \quad (16)$$

The 1st term of eqn (16) is the weighted averaged pressure of the nearest nodes surrounding the center point $\bar{r}=0$ while the 2nd term is accounting for the non-axisymmetric effect of sliding on the pressure distribution.

The boundary condition is illustrated in Fig. 2(b). On the boundary $\theta=0$ and $\theta=\pi$, reflective symmetry requires $\frac{\partial \bar{p}}{\partial \theta} = 0$ and $\frac{\partial \bar{u}}{\partial \theta} = 0$. Using centered difference scheme, we obtained the boundary value of \bar{p} and \bar{u} .

$$\frac{\bar{p}_{1,j} - \bar{p}_{-1,j}}{2\Delta\theta} = 0, \quad \frac{\bar{p}_{m+1,j} - \bar{p}_{m-1,j}}{2\Delta\theta} = 0; \quad \frac{\bar{u}_{1,j} - \bar{u}_{-1,j}}{2\Delta\theta} = 0; \quad \frac{\bar{u}_{m+1,j} - \bar{u}_{m-1,j}}{2\Delta\theta} = 0 \quad (17a)$$

$$\text{On the boundary } \bar{r} = 2, \text{ the pressure is zero, } \bar{p}_{i,n} = 0 \quad (17b)$$

It is known that negative pressure can occur near the exit region^{47,50}. In our simulations, this region as well as the magnitude of the negative pressure is found to be vanishing small for large β so this is not a serious physical concern. Nevertheless, in the results below we follow the conventional approach which is to eliminate this region of negative pressure by imposing the Reynolds condition. The Reynolds condition states that there exists a curve Γ at the downstream of the outlet region such that any point on Γ satisfies the condition that the pressure $\bar{P}(\bar{r}^*, \theta^*) = 0$ and $d\bar{P}(\bar{r}^*, \theta^*)/d\bar{h} = 0$ where \bar{h} is the in-plane normal vector of Γ . Additionally, downstream beyond Γ the pressure is zero everywhere. Enforcing the Reynolds condition is to disallow negative pressure anywhere. Numerically, at each iteration we set the pressure to be zero in the outlet region whenever it turns negative during the iterative solution. Results without imposing the Reynolds condition are given in the supporting information. In the ‘‘Hertz limit’’, the Reynolds condition only affects the pressure profile in a very small region near the outlet. In particular, it has no effect on the hydrodynamic friction.

2.4 Evaluation of the substrate surface displacement in polar coordinates

The conventional way to evaluate the surface displacement of the substrate, eqn (6b), is to approximate the continuous hydrodynamic pressure with an uniform distribution of pressure in each of small subdomains centered at each grid points. As pointed out in the introduction, calculation of the elastic deformation is computationally expensive. Some researchers tackle this difficulty using a method called ‘‘differential deflection’’^{35,51}. This method adds an additional layer of approximation since it accelerates the elasticity calculation by neglecting the contribution of far-field grid points. Our polar coordinates approach allows us to use the conventional and more accurate approach without running into computational difficulties. However, some non-trivial adjustments have to be made to evaluate eqn (6b). Specifically, unlike the uniform mesh in Cartesian coordinate where the subdomains are rectangles, the subdomains in our polar coordinates systems are irregular quadrilaterals. For any rectangular domain, the surface displacements due to a uniform pressure can be evaluated in closed form^{32,47}. The calculation of

surface displacement due to a uniform pressure acting on a quadrilateral is more complicated. Our procedure is summarized below.

Our method of computing the deformation of the substrate, eqn (6b), is shown schematically in Fig. 2. Basically, we need to calculate the surface deformation at any grid point, i.e. A , when there is a uniform pressure $P_{i,j}$ acting on a general quadrilateral, $BCDE$, around the grid point (i,j) . Note that the shape of quadrilateral is degraded to a triangle for those elements which share the node at $\bar{r} = 0$. This degradation is essentially a special case when the length of \overline{BE} is zero. For the general quadrilateral there is no closed form analytical solution to calculate the displacement. However, as shown in Fig. 3 one can always decompose the quadrilateral into the superposition of several right triangles for which the solution of full field displacement is available.

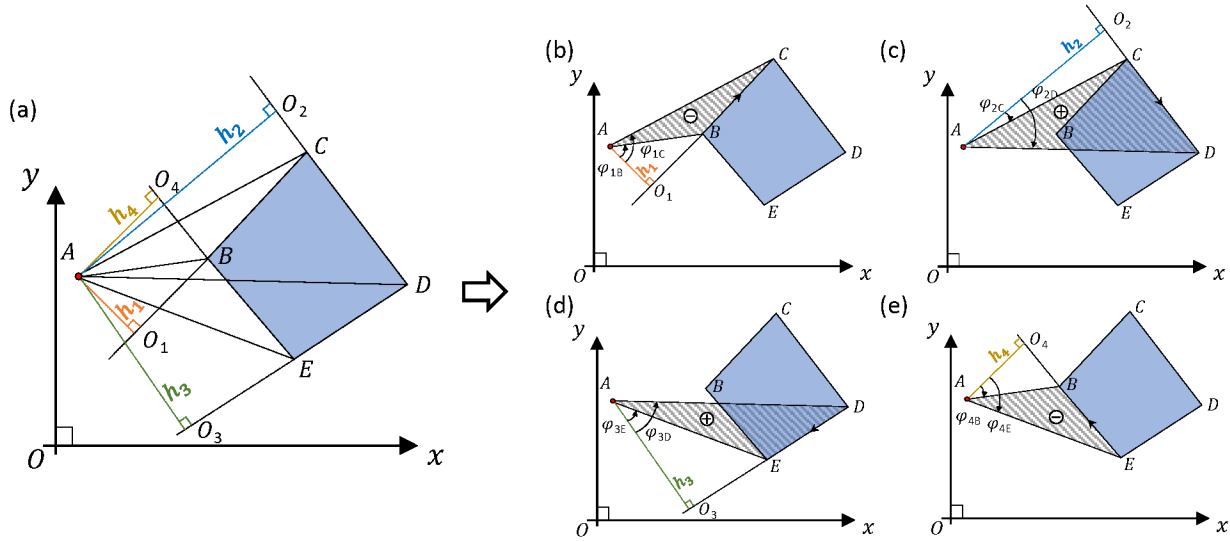


Fig. 3 (a) Aim to calculate the deformation of the point, A , when it is subjected to a uniform pressure distribution on the quadrilateral $BCDE$, $AO_1 \perp BC$, $AO_2 \perp CD$, $AO_3 \perp DE$, $AO_4 \perp EB$. (b~e) Decomposition of a general quadrilateral into superposition of four triangles, the sign indicates addition or subtraction in the superposition process.

The decomposition of a general quadrilateral into four triangles is shown in the Fig. 3. The quadrilateral $BCDE$ is $BCDE = -\Delta ACB + \Delta ADC + \Delta ADE - \Delta AEB$. The sign for each superposition of the triangle depends on the relative position of the target point A and the clockwise direction of each edge of the quadrilateral. When the target point is on the Left side of the edge vector, A to the edge vector \overline{BC} in Fig. 3(a) as an example, the sign should be negative while it should be positive if the target point is on the Right side of the edge vector as an example in Fig. 3(b). Each of the triangle $\Delta ACB, \Delta ADC, \Delta ADE, \Delta AEB$ consists of two right triangles. For example, $\Delta ACB = \Delta ACO_1 - \Delta ABO_1$. The vertical surface displacement field due to a uniform pressure acting on a right triangle on the surface of an elastic half space is given by Johnson⁴⁷. Take the right triangle ΔACO_1 and the general triangle ΔACB as examples, the deformation at A caused by uniform pressure P on these two triangles (the pressure is zero elsewhere) is:

$$w_{A, \Delta ACO_1} = \frac{P_{i,j} h_1}{8\pi G} \ln \left(\frac{1 + \sin \phi_{1C}}{1 - \sin \phi_{1C}} \right) \quad (18a)$$

$$w_{A,\Delta ACB} = \frac{P_{i,j} h_1}{8\pi G} \left[\ln \left(\frac{1 + \sin \varphi_{1C}}{1 - \sin \varphi_{1C}} \right) - \ln \left(\frac{1 + \sin \varphi_{1B}}{1 - \sin \varphi_{1B}} \right) \right] \quad (18b)$$

2.5 Iteration scheme

The numerical set up for the Reynolds and the elasticity equations is given in the previous section. The solution of the EHL problem requires the simultaneous solution of the Reynolds, eqn (6a), and the elasticity equations, eqn (6b). The nonlinearity of the Reynolds equation requires this to be done iteratively. The standard methods are: (i) relaxation method, (ii) the Newton-Raphson method. The relaxation method²⁹ is easy to implement and less memory-demanding, but usually requires more iterations to converge. The Newton-Raphson method^{27,52} requires much more memory but requires fewer iterations to converge. It is widely used in *line*-contact EHL problem because of the fast quadratic converge rate. However, the Newton-Raphson is proved to be inefficient when solving the point-contact EHL problem because of the huge non-sparse Jacobian matrix, which is difficult to handle numerically. Here we used the forward relaxation method²⁹ where the normalized pressure in the $\bar{p}_{i,j}^{(n+1)}$ iteration is related to the pressure in the n^{th} iteration $\bar{p}_{i,j}^{(n)}$ by

$$\bar{p}_{i,j}^{(n+1)} = \bar{p}_{i,j}^{(n)} + \lambda \left[F_{i,j} - A_{i,j} \bar{p}_{i-1,j}^{(n+1)} - B_{i,j} \bar{p}_{i,j-1}^{(n+1)} - C_{i,j} \bar{p}_{i,j}^{(n)} - D_{i,j} \bar{p}_{i,j+1}^{(n)} - E_{i,j} \bar{p}_{i+1,j}^{(n)} \right] / C_{i,j} \quad (19)$$

where λ is the relaxation factor.

Our numerical scheme is autonomous and requires no manual intervention. A flow chart of our numerical scheme is shown in Fig. 4. Briefly, in the numerical calculation we fix the vertical position of the sphere. We then provide a guess of the initial hydrodynamic pressure distribution. This initial guess should be a *continuously differentiable function of position* and this rules out the Hertz pressure. If the Hertz pressure is used as the initial guess, the numerical procedure oscillates and fails to converge. For the initial guess in our calculation, we used a 5th order polynomial function to approximate the Hertz pressure. This initial guess avoids the infinite gradient of the Hertz pressure domain at $\bar{r}=1$. The simulation starts with a small β_0 , for which it is easy to get a converged solution. The result is used as the next initial guess for a larger β . We used this process to march from small β_0 to the desired β , which is about 3 orders of magnitude larger. As β gets increasingly larger, the simulation tends to be unstable, which requires one to decrease the relaxation factor to stabilize the simulation. Typically, from $\beta_0=10$ to the $\beta=10000$, the relaxation factor λ decreases from 1.4 (over relaxation) to 0.1 (under relaxation). In our numerical scheme, we track the relative error $|\bar{p}_{new} - \bar{p}_{old}| / |\bar{p}_{old}|$ to check for convergence. If the relative error becomes too large, we reduce the relaxation factor by 60% percent and restart the simulation.

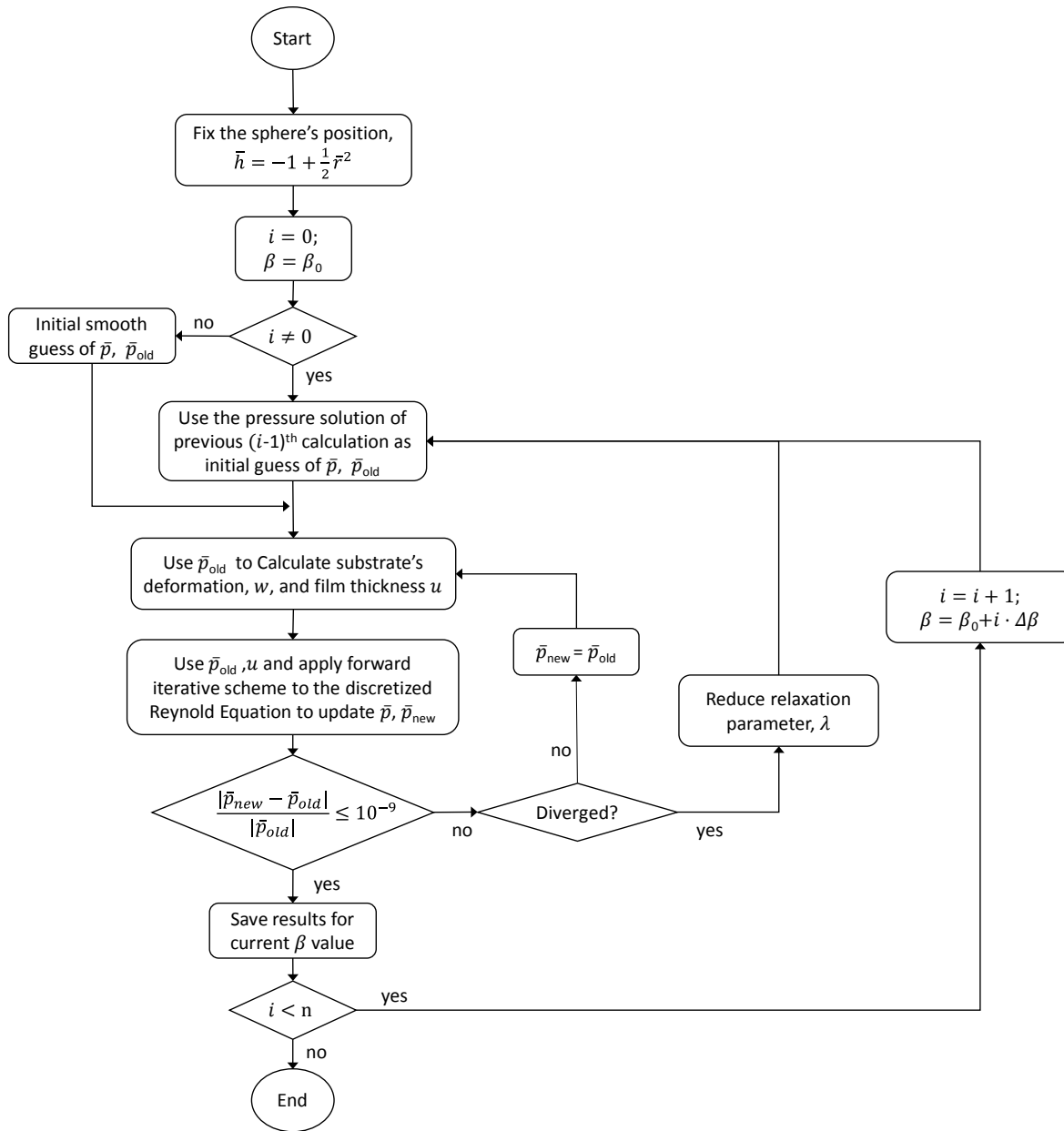


Fig. 4 Flow Chart of our numerical scheme

3. Results and Discussion.

3.1 Hydrodynamic pressure and scaling law for β

The pressure profiles along the x-axis and y-axis for different β are shown in Fig. 5. Also plotted is the Hertz pressure, eqn (7a). Fig. 5 shows that the pressure approaches the Hertz pressure as β increases. Increasing β means that more liquid is squeezed out under the indenter and the film thickness gets smaller. Fig. 5 shows that the pressure profile is smoother in the intake region than the exit - flow is slower in the intake region. In the iso-viscous EHL simulation, we did not observe any high pressure spike,

known as “Petrusevich Spike” near the exit. This spike is a feature of pressure dependent viscosity. The pressure profile over the whole calculation domain for different β value is shown in the SI.

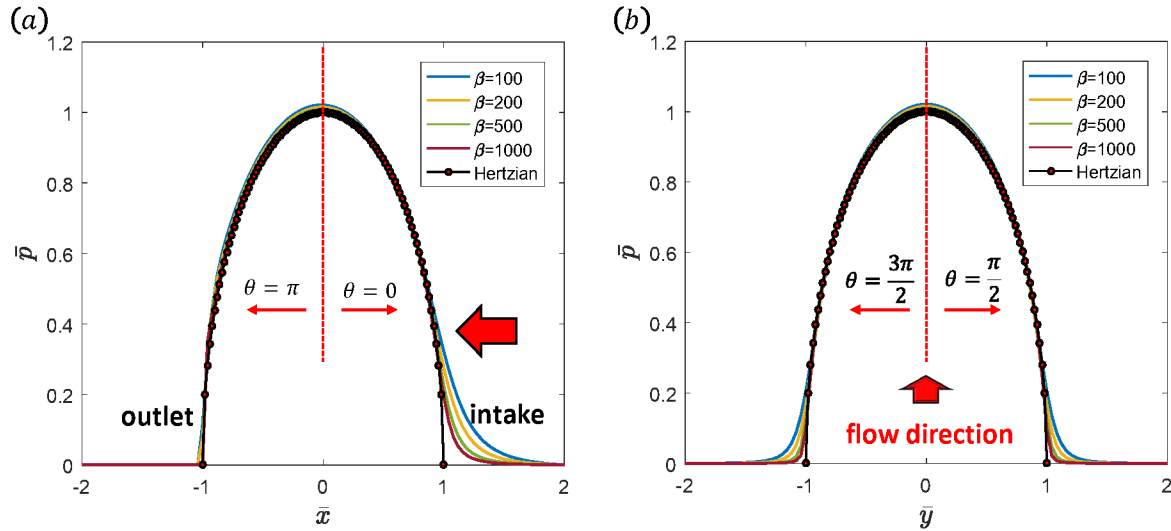


Fig. 5 Hydrodynamic Pressure profile at different cross-section; (a) cross-section along \bar{x} axis; (b) cross-section along \bar{y} axis. The results of different β value are presented, $\beta = 100, 200, 500, 1000$. The Hertzian solution is plotted as comparison.

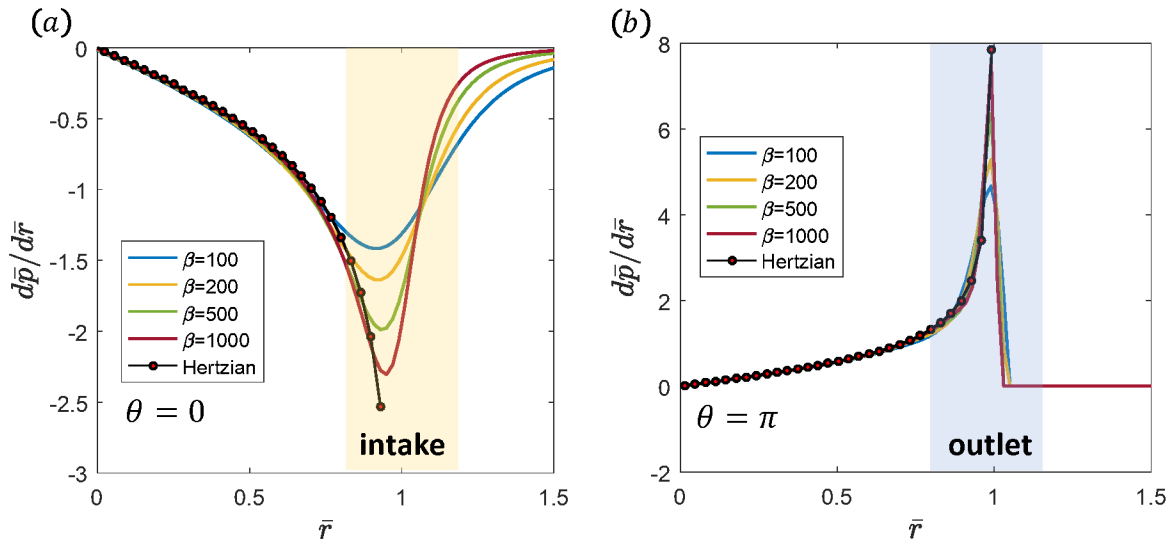


Fig. 6 Pressure gradient in (a) the intake region ($\theta = 0$) and (b) the outlet region ($\theta = \pi$). The results of different β value are presented, $\beta = 100, 200, 500, 1000$. The Hertzian solution is plotted as comparison.

The pressure gradient near the intake and outlet is shown in Fig. 6. Also plotted is the Hertz solution. Away from the intake or exit where $\bar{r} < 1$, the Hertz solution and the EHL solution for different β values all collapse onto each other. Near the intake or exit, the numerical solution and Hertz theory starts to diverge. In the intake region, the infinite pressure gradient predicted by Hertz's theory is regularized by liquid flow. In the outlet region, since the Reynolds condition was used to get rid of negative pressure, the pressure gradient of EHL solution has sharp peak near $\bar{r} \approx 1$.

As β increases, $|d\bar{p}/d\bar{r}|$ increases which results in larger intake velocity of the flow in this intake region. The maximum absolute pressure gradient value $|d\bar{p}/d\bar{r}|$ in the *intake region* versus different β value is shown in Fig. 7(a). Our numerical results show that:

$$\left|d\bar{p}/d\bar{r}\right|_{\max} = 0.5352\beta^{0.2112} \quad (20)$$

Next, we study the normalized thickness of the boundary layer, $\bar{\delta}$, at the intake region. We defined $\bar{\delta}$ as the distance between $\bar{r}=1$ and the position where $\bar{p}/\bar{p}_{\max}=0.05$. The relation between $\bar{\delta}$ and β is shown in Fig. 9(b). Our numerical result shows

$$\bar{\delta} = 4.216\beta^{-0.5077} \quad (21)$$

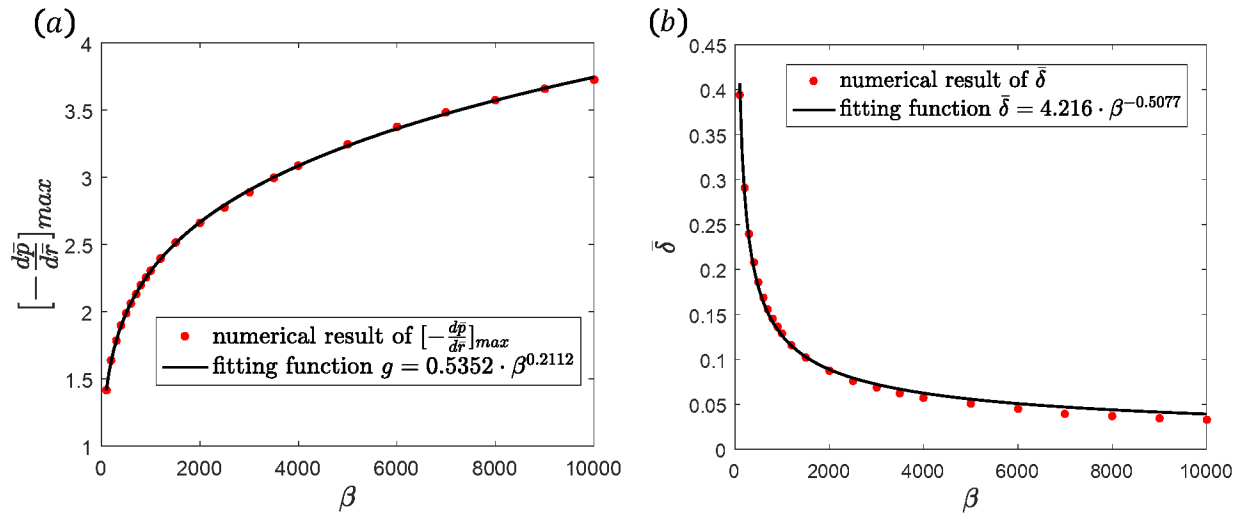


Fig.7 (a) Maximum absolute pressure gradient value $|d\bar{p}/d\bar{r}|$ in the intake region; (b) The normalized thickness of the boundary layer versus different β value.

3.2 Film thickness

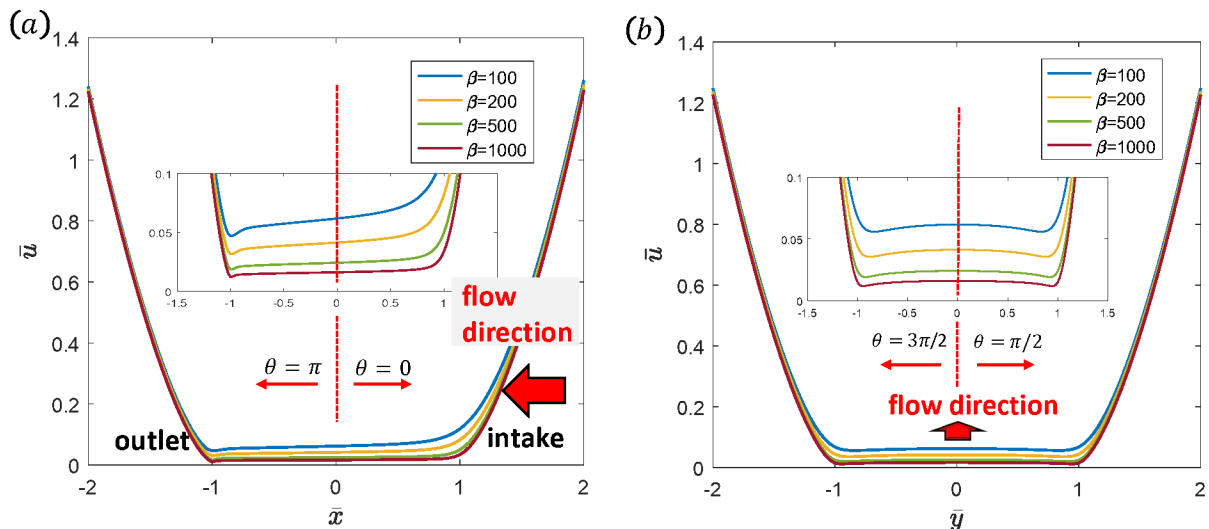


Fig. 8 Film thickness profile at different cross-section; (a) cross-section along \bar{x} axis; (b) cross-section along \bar{y} axis. The results of different $\beta = 100, 200, 500, 1000$ are presented. The imbedded figures show details of the film thickness at the ‘Hertz’ contact region.

The profile of the liquid film thickness along the x-axis and y-axis for different β is shown in the Fig. 8. In the “contact” region $\bar{r} < 1$, the thickness of the liquid film is largest at the center $\bar{r} = 0$ and decreases very slowly until \bar{r} reaches the intake and exit regions. In particular, the film thickness at the intake region is noticeably larger than the exit region where the liquid flows rapidly, due to the rapid decrease of hydrodynamic pressure. The normalized film thickness at the center of the sphere \bar{u}_{mid} and the minimum normalized film thickness \bar{u}_{min} at the outlet were extracted from our numerical results and plotted in Fig. 10. These thicknesses obey the following scaling laws shown in eqn (22a,b).

$$\begin{aligned}\bar{u}_{mid} &= 0.9051\beta^{-0.5826} \\ \bar{u}_{min} &= 0.9283\beta^{-0.6626}\end{aligned}\quad (22a,b)$$

Contour plots of the film thickness in the contact region ($\bar{r} \leq 1$) for different β are shown in the Fig. 9. Liquid enters into the contact region from the positive x direction. As expected, the film thickness is thinner at the region where the fluid exits. To further check our numerical results, we compare the normalized film thickness at the inlet region $\bar{r} - 1 = 0, \theta = 0$ with the result of Snoeijer et al⁴⁶. There is excellent agreement between the two results. This comparison is given in the supplementary information.

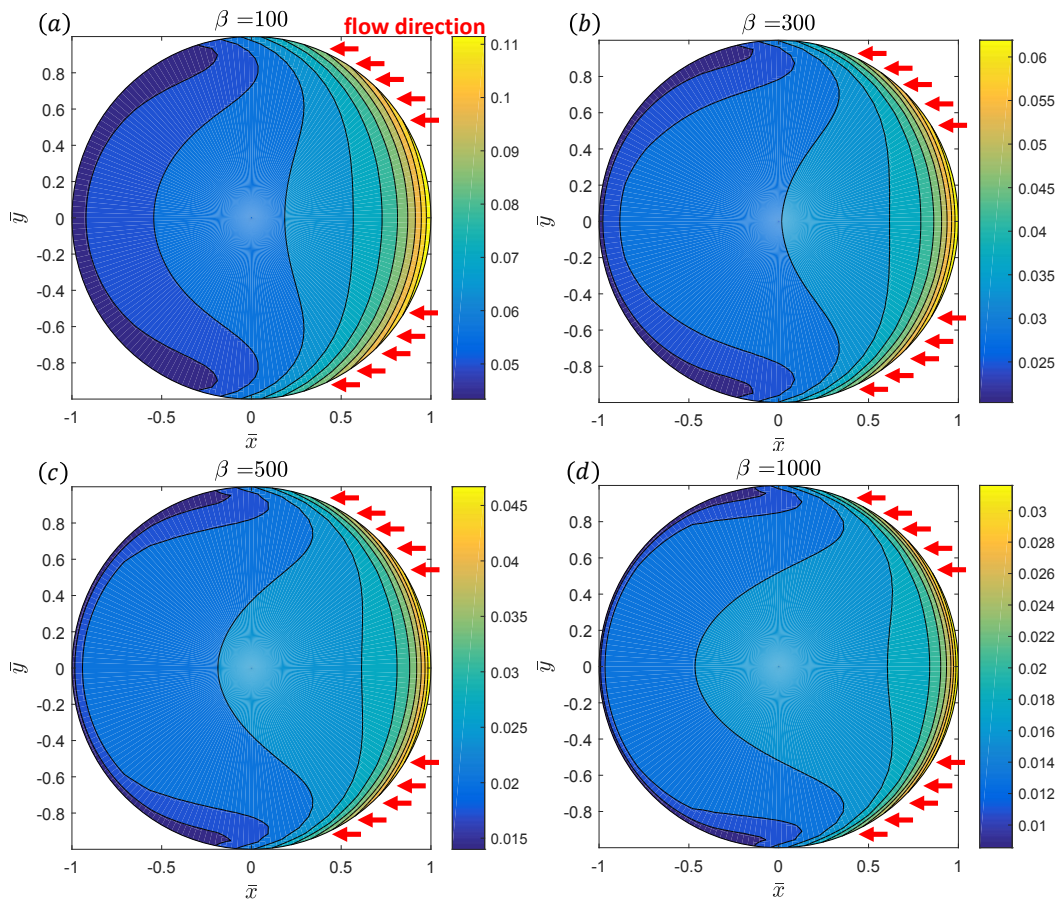


Fig. 9 Film thickness contour in the Hertzian contact region $\bar{r} \leq 1$ for different β value. (a) $\beta = 100$, (b) $\beta = 300$, (c) $\beta = 500$, (d) $\beta = 1000$.

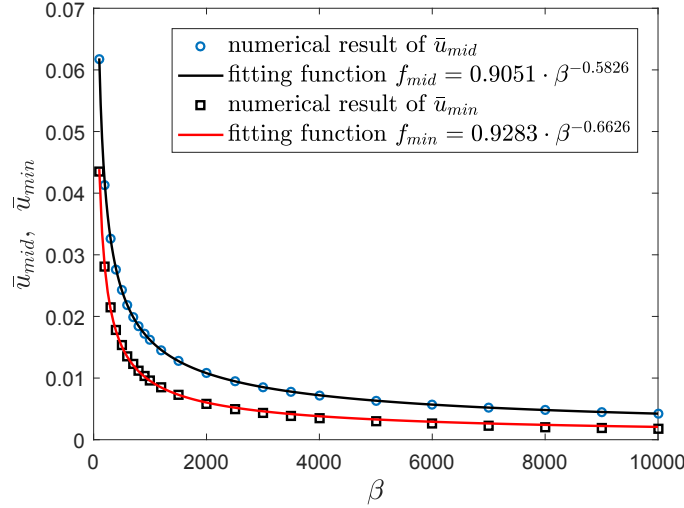


Fig. 10 Dependence of liquid film thickness at $\bar{r} = 0$ (\bar{u}_{mid}) and minimum film thickness (\bar{u}_{min}) on β . Fitting functions for \bar{u}_{mid} , \bar{u}_{min} are also plotted.

3.3 Velocity field

Our recent work has shown that small fluorescent particles can be used to capture the fluid velocity field during sliding¹⁷. Since the flow velocities are proportional to the pressure gradient, this particle tracking method allows indirect measurement of the hydrodynamic pressure. In Reynolds theory, the normalized velocities and pressure gradients are related by

$$\bar{v}_r = 3\beta(\bar{z} - \bar{w})(\bar{z} - \bar{h})\bar{p}_{,r} + \frac{\bar{z} - \bar{w}}{\bar{u}} \cos\theta \quad (23a)$$

$$\bar{v}_\theta = 3\beta(\bar{z} - \bar{w})(\bar{z} - \bar{h})\frac{1}{\bar{r}}\bar{p}_{,\theta} - \frac{\bar{z} - \bar{w}}{\bar{u}} \sin\theta \quad (23b)$$

Where $\bar{v}_r = v_r / v$, $\bar{v}_\theta = v_\theta / v$ and \bar{z} is the normalized position of the plane where the velocity field is measured. The average velocities are obtained by integrating through the film thickness, i.e.,

$$\bar{v}_{r,ave} \equiv \frac{\int_{\bar{w}}^{\bar{h}} \bar{v}_r \cdot dz}{\int_{\bar{w}}^{\bar{h}} dz} = -\frac{1}{2}\beta\bar{p}_{,r}\bar{u}^2 + \frac{1}{2}\cos\theta ; \quad (24a)$$

$$\bar{v}_{\theta,ave} \equiv \frac{\int_{\bar{w}}^{\bar{h}} \bar{v}_\theta \cdot dz}{\int_{\bar{w}}^{\bar{h}} dz} = -\frac{1}{2\bar{r}}\beta\bar{p}_{,\theta}\bar{u}^2 - \frac{1}{2}\sin\theta \quad (24b)$$

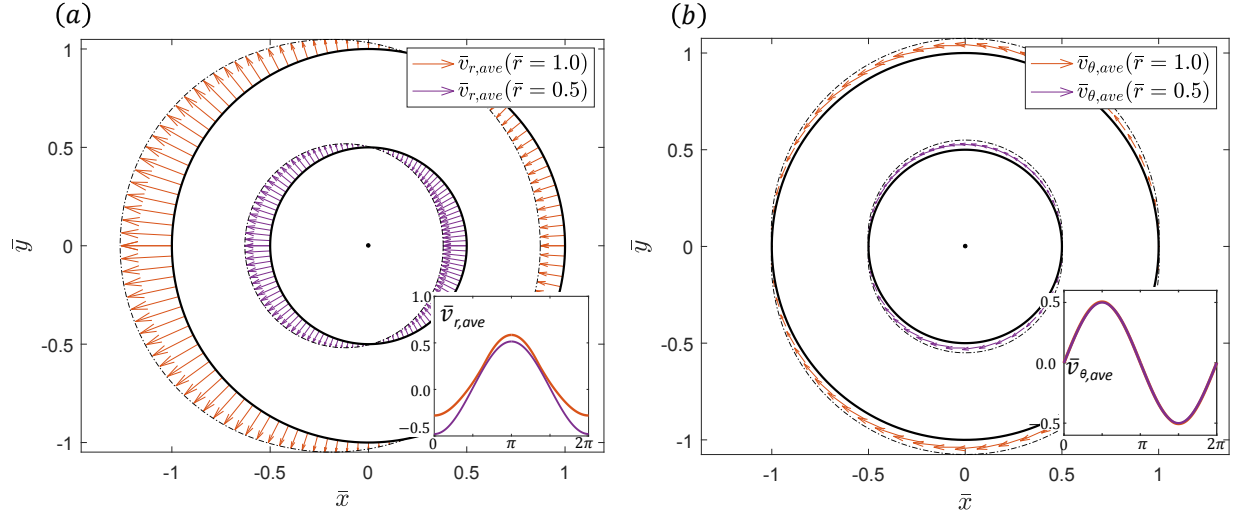


Fig. 11 Components of the average velocity of the flow flowing into the two rings $\bar{r} = 0.5$ and $\bar{r} = 1.0$ (a) the averaged radial flow velocity $\bar{v}_{r,ave}$; (b) the averaged swirl flow velocity $\bar{v}_{\theta,ave}$.

Fig. 11 plots the average velocities field $(\bar{v}_{r,ave}, \bar{v}_{\theta,ave})$ on the circles $\bar{r} = 0.5$ and $\bar{r} = 1.0$. For the averaged radial component $\bar{v}_{r,ave}$, the velocity of the flow entering the circle $\bar{r} = 1.0$ is smaller than that exiting the ring. This is because the liquid film is thicker in the intake region. However, for $\bar{r} = 0.5$, the flow velocity entering and exiting the ring is practically the same since the film thickness varies but little. For the averaged swirl velocity component $\bar{v}_{\theta,ave}$, Fig. 11(b) shows that the velocities on both circles are similar. The magnitude of $\bar{v}_{\theta,ave}$ versus θ is a sinusoidal function. The flow splits at $\theta = 0$ and meet at $\theta = \pi$. As expected, $\bar{v}_{\theta,ave}$ reaches its maximum at $\theta = \pi/2, 3\pi/2$.

3.4 Hydrodynamic friction F_f

The shear traction between the sphere and the liquid layer gives rise to hydrodynamic friction F_f . Due to reflection symmetry, only the shear traction component τ_{zx} contributes to the hydrodynamic friction. This stress component is:

$$\tau_{zx} \equiv \eta \frac{\partial v_x}{\partial z} \Rightarrow \bar{\tau}_{zx} = \frac{\partial \bar{v}_x}{\partial \bar{z}} = 3\beta \bar{\rho}_{,x} (2\bar{z} - \bar{h} - \bar{w}) + \frac{1}{\bar{u}} \quad (25)$$

where $\bar{\tau}_{zx} = \frac{|h_0|}{\nu\eta} \tau_{zx} = \sqrt{\frac{3}{2} \frac{R}{\pi\nu\eta G}} \beta \tau_{zx}$ is the normalized shear stress and \bar{u} is the normalized film thickness.

Since the average through thickness $\bar{\tau}_{zx}$ depends only on β , the average through thickness shear stress must be given by $(\eta\nu G/R)^{1/2} f(\beta)$ where f is a function that depends only on β . This is consistent with the results of Meeker et al.,^{53,54}. In the following, we denote the normalized the hydrodynamic friction by

$$\bar{F}_f = \frac{3F_f}{2\pi G h_0^2} \quad (26)$$

The normalized hydrodynamic friction and normal force are determined by integrating τ_{zx} and the hydrodynamic pressure over $r \leq \alpha_H$. In normalized form, we have:

$$\bar{F}_f \equiv \frac{1}{\beta} \iint_{\bar{r} \leq 1} \bar{\tau}_{zx} \Big|_{\bar{z}=\bar{h}} d\bar{x}d\bar{y} = \iint_{\bar{r} \leq 1} \left[3\bar{p}_{,x} \bar{u} + \frac{1}{\beta \bar{u}} \right] d\bar{x}d\bar{y} \quad (27a)$$

$$\bar{N} \equiv \iint_{\bar{r} \leq 1} \bar{p} d\bar{x}d\bar{y} \quad (27b)$$

Eqn (27a,b) state that \bar{F}_f and the normalized normal force \bar{N} depend on the single parameter β . Hence there is an universal relation between these quantities. The normalized friction force \bar{F}_f and the applied normal force \bar{N} versus β are plotted in Fig. 12. As β increases the normalized normal force \bar{N} is independent of β . This is expected since the normal force must converge to the Hertz normal force. This is because the contribution of the boundary layer to the normal force is insignificant as the thickness of the boundary layer vanishes as β goes to infinity. Indeed, according to eqn (4,5b), $\bar{N}(\beta \gg 1)$ should approach $4/3\pi$, as confirmed by our result in Fig. 12. The blue curve in Fig. 12 shows that the normalized friction force obeys the scaling law eqn (28).

$$\bar{F}_f = 4.806\beta^{-0.4398} \quad \beta \gg 1 \quad (28)$$

Since the normal load N is given by the Hertz solution for $\beta \gg 1$, we must have:

$$|h_0| = \left[\frac{3N}{16G\sqrt{R}} \right]^{2/3} \quad (29)$$

Thus, β in this regime can also be expressed in terms of the normal load as:

$$\beta = \frac{2}{3} \frac{h_0^2}{R} \frac{\pi G}{\eta v} = \frac{2}{3} \frac{\pi G}{\eta R v} \left[\frac{3N}{16G\sqrt{R}} \right]^{4/3} = \frac{2\pi}{3} \left[\frac{3}{16} \right]^{4/3} \frac{N^{4/3}}{\eta G^{1/3} R^{5/3} v} \quad (30)$$

This expression for β is useful for sliding experiments carried out with a fixed normal force (instead of a fixed normal displacement).

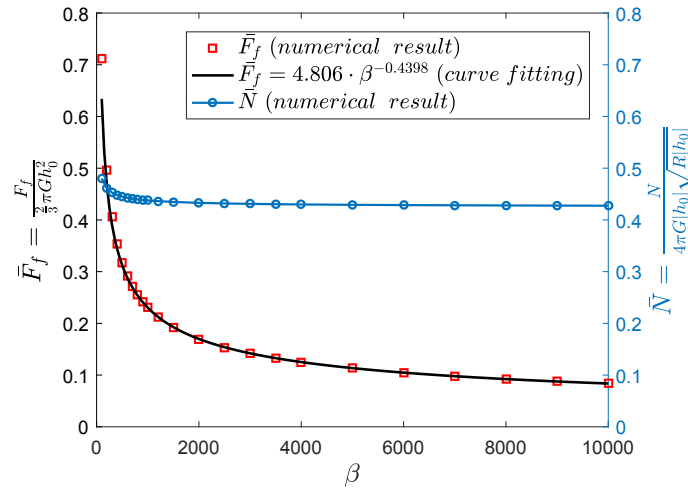


Fig. 12 Normalized friction and Normal force versus β .

3.5 Comparison with experiments

For experimental analysis, samples were fabricated using poly(dimethylsiloxane) (PDMS, Dow Sylgard 184, Dow Corning) with a 10:1 base to cross linker ratio. Samples were cast as flat 2mm thick slabs, with a Young's modulus of approximately 3MPa. Sliding experiments were completed using a spherical glass indenter as the contacting surface ($R=2\text{ mm}$) and PDMS base as the lubricant due to its wetting properties. Experiments were performed using normal loads ranging from 18.6 to 238.1mN and sliding velocities ranging from 0.025 to 1mm/s, with a total of 72 load and velocity combinations tested. The scaled results of these experiments are plotted in Fig. 13, where they collapse onto one master curve. Also plotted is the numerical prediction using eqn (28). The experiments and the numerical results show excellent agreement. The experimental data in Fig 13 used a viscosity value for PDMS base, η , of $2Pa \cdot s$ in order for the data to best match the theory. This viscosity is somewhat lower than the manufacturer's reported value of about $5Pa \cdot s$. The difference might be caused by the fact that the viscosity is quite sensitive to temperature.

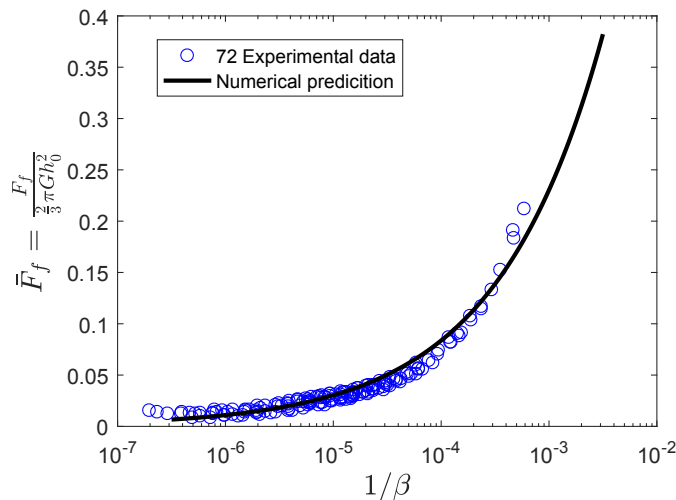


Fig. 13 Comparison of experimental data with numerical prediction using eqn(28)

4. Summary and discussion

A detailed analysis is carried out to study the lubricated steady sliding of a rigid sphere on an infinite elastic substrate. In contrast to most of previous works, we assume pressure independent viscosity, which is a reasonable assumption in EHL problem for typical soft substrate. The solution of the EHL problem in this regime is determined by a single dimensionless parameter β which can be interpreted as the inverse of a normalized sliding velocity. Our focus is on the ‘‘Hertz’’ limit where $\beta \gg 1$. This corresponds to large normal load, small viscosity and slow sliding speed. This regime is known to present numerical difficulties. We have developed a new numerical scheme to overcome these difficulties – our scheme can handle β as large as 10^4 . Our scheme uses polar coordinates, which reduces the computation time. The use of a non-uniform mesh in the radial direction near the inlet and outlet region also increases accuracy. Our scheme is autonomous and requires no manual intervention. Using this scheme, we studied in detail the structure of the hydrodynamic pressure and flow field near the inlet and outlet region. The dependence of pressure gradient, film thickness and size of boundary layer on β is given in closed form. These universal scaling laws give important insight to the flow mechanics in this highly confined regime. Our calculation allows us to determine the dependence of hydrodynamic friction on β . We check this dependence against our recent experiments and find excellent agreement.

The numerical formulation and numerical scheme presented in this work can be used to simulate a wide variety of point-contact EHL problems, such as indentation of a sphere into an elastic layer covered with liquid layer, sliding a sphere in lubricant with pressure-sensitive viscosity and so on. Our scheme is well suited to study the large force, small sliding velocity regime where conventional numerical methods tend to be unreliable.

Appendix

1. Asymptotic behavior of solution for far field $\bar{r} \gg 1$

For the far field where $\bar{r} \gg 1$, we expect that the pressure and displacement goes to zero, so that:

$$\bar{h} - \bar{w} = \bar{u} \approx \bar{h} = \bar{h}_0 + \frac{\bar{r}^2}{2} \approx \frac{\bar{r}^2}{2}, \quad \bar{r} \gg 1 \quad (\text{A1})$$

Substituting eqn (A1) into (6a) and neglecting the variation of \bar{u} in θ direction, the eqn (6a) reduces to:

$$\frac{\partial}{\partial \bar{r}} \left(\bar{r}^7 \frac{\partial \bar{p}}{\partial \bar{r}} \right) + \frac{\partial}{\partial \theta} \left(\bar{r}^5 \frac{\partial \bar{p}}{\partial \theta} \right) = -\frac{8\bar{r}^2 \cos \theta}{\beta} \quad (\text{A2})$$

A solution of the form: $\bar{p} = A\bar{r}^{-3} \cos \theta$, would satisfy the (A2). The coefficient is easy to obtain. It turns out that the far field pressure $\bar{p}(\bar{r} \gg 1)$ is completely determined by the Reynolds equation and is independent of elasticity.

$$\bar{p} = \frac{4}{5\beta} \bar{r}^{-3} \cos \theta, \quad \bar{r} \gg 1 \quad (\text{A3})$$

2. Coefficient of the discretized Reynolds equation, eqn (13)

The coefficients of the discretized form of the Reynolds equation, eqn (13), is shown in eqn (A4a~f). Note that the $A_{i,j}$, $B_{i,j}$, $C_{i,j}$, $D_{i,j}$, $E_{i,j}$ and $F_{i,j}$ are functions of the mesh grid size, the grid position, film thickness and β . These coefficients need to be updated in each iteration of solving eqn (13).

$$A_{i,j} = \frac{\bar{u}_{i,j}^2}{r_j^2 (\Delta\theta)^2} \left[\bar{u}_{i,j} - \frac{3}{4} (\bar{u}_{i+1,j} - \bar{u}_{i-1,j}) \right] \quad (\text{A4a})$$

$$B_{i,j} = -\frac{\bar{u}_{i,j}^3}{r_j d_j (1+\lambda_j)} + \frac{2\lambda_j \bar{u}_{i,j}^3}{d_j d_{j-1} (1+\lambda_j)} - \frac{3\lambda_j^2 \bar{u}_{i,j}^2}{d_j^2 (1+\lambda_j)^2} \left[\bar{u}_{i,j+1} - \lambda_j^2 \bar{u}_{i,j-1} - (1-\lambda_j^2) \bar{u}_{i,j} \right] \quad (\text{A4b})$$

$$C_{i,j} = -\frac{(1-\lambda_j) \bar{u}_{i,j}^3}{r_j d_j} - \frac{2\bar{u}_{i,j}^3}{d_j d_{j-1}} - \frac{3\bar{u}_{i,j}^2 (1-\lambda_j)}{d_j^2 (1+\lambda_j)} \left[\bar{u}_{i,j+1} - \lambda_j^2 \bar{u}_{i,j-1} - (1-\lambda_j^2) \bar{u}_{i,j} \right] - \frac{2\bar{u}_{i,j}^3}{r_j^2 (\Delta\theta)^2} \quad (\text{A4c})$$

$$D_{i,j} = \frac{\bar{u}_{i,j}^3}{r_j d_j (1+\lambda_j)} + \frac{2\bar{u}_{i,j}^3}{d_j d_{j-1} (1+\lambda_j)} + \frac{3\bar{u}_{i,j}^2}{d_j^2 (1+\lambda_j)^2} \left[\bar{u}_{i,j+1} - \lambda_j^2 \bar{u}_{i,j-1} - (1-\lambda_j^2) \bar{u}_{i,j} \right] \quad (\text{A4d})$$

$$E_{i,j} = \frac{\bar{u}_{i,j}^2}{r_j^2 (\Delta\theta)^2} \left[\bar{u}_{i,j} + \frac{3}{4} (\bar{u}_{i+1,j} - \bar{u}_{i-1,j}) \right] \quad (\text{A4e})$$

$$F_{i,j} = -\frac{1}{\beta} \left[\cos\theta_i \left(\frac{\bar{u}_{i,j+1} - \lambda_j^2 \bar{u}_{i,j-1} - (1-\lambda_j^2) \bar{u}_{i,j}}{d_j (1+\lambda_j)} \right) - \frac{\sin\theta_i}{r_j} \left(\frac{\bar{u}_{i+1,j} - \bar{u}_{i-1,j}}{2\Delta\theta} \right) \right] \quad (\text{A4f})$$

Conflicts of interest

There are no conflicts of interest to declare.

Acknowledgements

We acknowledge the support from the National Science Foundation, primarily by CMMI-1538002 and in part by CMMI-1854572. We thank two anonymous reviewers for their valuable suggestions.

References

- 1 A. (Alastair) Cameron, *Basic lubrication theory*, E. Horwood, 1976.

- 2 D. Dowson, G. R. Higginson, J. F. Archard and A. W. Crook, *Elasto-hydrodynamic lubrication*, Pergamon Press, 1977.
- 3 B. N. J. Persson, *Sliding Friction, Physical Principles and Applications*, Springer-Verlag, 2nd Editio., 2000.
- 4 E. H. Okrent, *ASLE Transactions*, 1961, **4**, 97–108.
- 5 S. T. Tzeng and E. Saibel, *ASLE Transactions*, 1967, **10**, 334–348.
- 6 B. L. S. Martz, *Proceedings of the Institution of Mechanical Engineers*, 1947, **16**, 1–9.
- 7 J. A. Mcgeehan, in *SAE Technical Paper Series*, 1978, vol. 1.
- 8 B. N. J. Persson and M. Scaraggi, *Journal of Physics Condensed Matter*, 2009, **21**, 185002.
- 9 M. Scaraggi, G. Carbone, B. N. J. Persson and D. Dini, *Soft Matter*, 2011, **7**, 10395–10406.
- 10 M. Scaraggi, G. Carbone and D. Dini, *Soft Matter*, 2011, **7**, 10407.
- 11 J. M. Skotheim and L. Mahadevan, *Physics of Fluids*, 2005, **17**, 1–23.
- 12 B. Saintyves, T. Jules, T. Salez and L. Mahadevan, *Proceedings of the National Academy of Sciences*, 2016, **113**, 5847–5849.
- 13 Y. Wang, C. Dhong and J. Frechette, *Physical Review Letters*, 2015, **115**, 248302.
- 14 Y. Wang, M. R. Tan and J. Frechette, *Soft Matter*, 2017, **13**, 6718–6729.
- 15 F. Kaveh, J. Ally, M. Kappl and H. J. Butt, *Langmuir*, 2014, **30**, 11619–11624.
- 16 S. Leroy, A. Steinberger, C. Cottin-Bizonne, F. Restagno, L. Léger and I. Charlaix, *Physical Review Letters*, 2012, **108**, 264501.
- 17 N. Moyle, H. Wu, C. Khripin, F. Bremond, C.-Y. Hui and A. Jagota, *Soft Matter*, 2020, 10.1039.C9SM02087J.
- 18 J. De Vicente, J. R. Stokes and H. A. Spikes, *Tribology Letters*, 2005, **20**, 273–286.
- 19 J. H. H. Bongaerts, K. Fourtouni and J. R. Stokes, *Tribology International*, 2007, **40**, 1531–1542.
- 20 C. Myant, H. A. Spikes and J. R. Stokes, *Tribology International*, 2010, **43**, 55–63.
- 21 M. Scaraggi, G. Carbone and D. Dini, *Tribology Letters*, 2011, **43**, 169–174.
- 22 J. M. Kim, F. Wolf and S. K. Baier, *Tribology International*, 2015, **89**, 46–53.
- 23 S. Stupkiewicz, J. Lengiewicz, P. Sadowski and S. Kucharski, *Tribology International*, 2016, **93**, 511–522.
- 24 N. Selway, V. Chan and J. R. Stokes, *Soft Matter*, 2017, **13**, 1702–1715.
- 25 P. Sadowski and S. Stupkiewicz, *Tribology International*, 2019, **129**, 246–256.
- 26 *Proceedings of the Royal Society of London*, 1886, **40**, 191–203.
- 27 K. P. Oh and S. M. Rohde, *Int. J. Numer. Meth. Engng.*, 1977, **11**, 1507–1518.
- 28 D. Dowson and G. R. Higginson, *Journal of Mechanical Engineering Science*, 1959, **1**, 6–15.
- 29 B. J. Hamrock and D. Dowson, *Journal of Lubrication Technology*, 1976, **98**, 223.
- 30 B. J. Hamrock and D. Dowson, *Journal of Lubrication Technology*, 1976, **98**, 375.
- 31 B. J. Hamrock and D. Dowson, *Journal of Lubrication Technology*, 1977, **99**, 264.
- 32 D. Dowson and B. J. Hamrock, *ASLE Transactions*, 1976, **19**, 279–286.
- 33 S. Biswas and R. W. Snidle, *J. Lub. Tech.*, 1977, **99**, 313.
- 34 H. P. Evans and T. G. Hughes, *Proceedings of the Institution of Mechanical Engineers, Part C: Journal of Mechanical Engineering Science*, 2000, **214**, 563–584.
- 35 T. G. Hughes, C. D. Elcoate and H. P. Evans, *Proceedings of the Institution of Mechanical Engineers, Part C: Journal of Mechanical Engineering Science*, 2000, **214**, 585–598.
- 36 *Journal of the American Society for Naval Engineers*, 2009, **67**, 51–68.
- 37 H. P. Evans, *J. Tribol.*, 1981, **103**, 547.
- 38 H. P. Evans, *J. Tribol.*, 1981, **103**, 539.

- 39 H. P. Evans and R. W. Snidle, *Proceedings of the Royal Society A: Mathematical, Physical and Engineering Sciences*, 1982, **382**, 183–199.
- 40 A. P. Ranger, C. M. M. Ettles and A. Cameron, *Proceedings of the Royal Society A: Mathematical, Physical and Engineering Sciences*, 1975, **346**, 227–244.
- 41 B. J. Hamrock and D. Dowson, *Journal of Lubrication Technology*, 1977, **99**, 15.
- 42 B. N. J. Persson, *Sliding Friction*, Springer Berlin Heidelberg, Berlin, Heidelberg, 2000.
- 43 C. Putignano, *Journal of the Mechanics and Physics of Solids*, 2020, **134**, 103748.
- 44 A. Daddi-Moussa-Ider, B. Rallabandi, S. Gekle and H. A. Stone, *Phys. Rev. Fluids*, 2018, **3**, 084101.
- 45 B. Rallabandi, B. Saintyves, T. Jules, T. Salez, C. Schönecker, L. Mahadevan and H. A. Stone, *Phys. Rev. Fluids*, 2017, **2**, 074102.
- 46 J. H. Snoeijer, J. Eggers and C. H. Vennert, *Physics of Fluids*, 2013, **25**, 101705.
- 47 K. L. Johnson, *Contact Mechanics*, Cambridge University Press, Cambridge, 1985.
- 48 Y.-Y. Lin and H.-Y. Chen, *J. Polym. Sci. B Polym. Phys.*, 2006, **44**, 2912–2922.
- 49 H. Sundqvist and G. Veronis, *Tellus*, 1970, **22**, 26–31.
- 50 V. Kumar, *Wear*, 1981, **65**, 295–306.
- 51 M. J. A. Holmes, H. P. Evans, T. G. Hughes and R. W. Snidle, *Proceedings of the Institution of Mechanical Engineers, Part J: Journal of Engineering Tribology*, 2003, **217**, 289–304.
- 52 S. M. Rohde and K. P. Oh, *Proceedings of the Royal Society A: Mathematical, Physical and Engineering Sciences*, 1975, **343**, 315–331.
- 53 S. P. Meeker, R. T. Bonnecaze and M. Cloitre, *Phys. Rev. Lett.*, 2004, **92**, 198302.
- 54 S. P. Meeker, R. T. Bonnecaze and M. Cloitre, *Journal of Rheology*, 2004, **48**, 1295–1320.